G. Purpura, P. Di Lizia
Autonomous GNC Strategy for an Asteroid Impactor Mission
CEAS Space Journal, Vol. 13, 2021, p. 65-81
doi:10.1007/s12567-020-00325-5

Noname manuscript No.
(will be inserted by the editor)

Autonomous GNC strategy for an asteroid impactor mission

Giovanni Purpura · Pierluigi Di Lizia

Received: date / Accepted: date

Abstract The Solar System features thousands of Near-Earth Asteroids that could be at collision risk with our planet in the future. Scientists are investigating the possibility of deflecting asteroids from their trajectory by means of a hyper-velocity impactor spacecraft. The aim of this research is to develop and simulate a GNC strategy to control the spacecraft towards its impact with the asteroid. The navigation is based on the use of a camera to estimate the relative position through image analysis and a filtering process. A zero-effort error strategy is adopted for the control. A simulator has been developed to render the simulated images online and test the GNC algorithms. The simulator is used to assess the performance of the strategy on different scenarios and to perform a sensitivity analysis with respect to the environmental and design parameters.

Keywords asteroid · deflection · impactor · NEA · Guidance Navigation and Control

1 Introduction

The Solar System features thousands of Near-Earth Asteroids (NEA). Some of them could potentially have a collision with our planet in the future. The scientific community is currently investigating the possible actions to avert this event, which could

G. Purpura
Politecnico di Milano
Department of Aerospace Science and Technology
Milan, Italy
ORCiD: 0000-0001-6136-3487
E-mail: giovanni.purpura@polimi.it

P. Di Lizia
Politecnico di Milano
Department of Aerospace Science and Technology
Milan, Italy
ORCiD: 0000-0003-1692-3929
E-mail: pierluigi.dilizia@polimi.it

lead to a catastrophic outcome. A possible strategy that is being considered is the deflection of the asteroid from its trajectory by impacting it with a spacecraft at very high velocity.

Several missions to asteroids or comets have already been launched or are currently under study by the major space agencies. A brief description of the missions relevant to this work is provided hereafter, including details on their navigation strategy.

JAXA Hayabusa [11] was an exploration mission to asteroid 25143 Itokawa. It had autonomous optical navigation, using a target marker previously released on the asteroid. The camera image was processed using maximum correlation shifting and FFT. The adopted control strategy allowed the spacecraft to approach the asteroid from preset directions.

NASA Deep Impact [10] was an hypervelocity asteroid impact vehicle to comet Tempel 1. It used AutoNav, a software developed for the previous mission Deep Space 1, for guidance, navigation and control (GNC). The software is able to perform image processing, orbit determination and maneuver computation. The image was processed by brightness centroiding, blobbing and scene analysis for site selection. It featured pulsed predictive control.

ESA Don Quijote [2] was a space probe concept to impact a NEA and determine the resulting momentum transfer. It was composed of an orbiter and an impactor. The orbiter could also perform surface analysis and mapping. It featured autonomous optical navigation for the impactor. The mission was eventually canceled in favor of AIDA mission.

ESA/NASA Asteroid Impact and Deflection mission (AIDA) [7] is a proposed pair of probes that would demonstrate an impact to change the motion of the binary NEA Didymos. NASA DART probe would impact the smallest body with the aid of a camera changing the speed by a fraction of 1 %. ESA Hera mission would arrive at Didymos five years later to study the asteroid and measure the effects of the impact.

A joint initiative between space agencies and other institutions was initiated in 2013 to prepare an international response to an asteroid impact threat. As a result, the Space Mission Planning Advisory Group (SMPAG) was established [6]. A preliminary work performed by the Italian Space Agency for SMPAG, which was aimed at defining and analyzing a test scenario for a deflection mission, was presented by Colombo et al. [3]. The chosen target for simulations is 2010 RF_{12}, a small NEA with significant probability of hitting the Earth. The work considered an asteroid in the orbit of 2010 RF_{12} with increased mass and diameter. The outcome of the work was an optimal impact orbit and a preliminary sizing of the components of the spacecraft.

Orbital insertion maneuvers are subjected to errors, therefore the spacecraft has to be controlled towards the target during the final phase of the mission. Since the camera can detect the asteroid only few hours before the impact, it is mandatory that GNC is performed autonomously. This paper aims at introducing an autonomous GNC strategy for the mission scenario defined in [3].

The paper is organized as follows. The dynamics of the asteroid and the spacecraft are described in Sec. 2. Sec. 3 presents the estimation process for the translational and rotational states by means of Kalman filters, focusing on the navigation camera and on

the image analysis algorithm. The control strategy that allows the spacecraft to correct its course in order to impact the asteroid is defined in Sec. 4. Attitude control to keep the camera pointing towards the asteroid is introduced in Sec. 5. The defined equations and algorithms are used to develop a software simulator using MATLAB®, Simulink® and Blender®; the results of the simulations are reported in Sec. 6. In conclusion, the feasibility of the mission is discussed in Sec. 7, highlighting the reached goals and outlining the necessary future work.

2 Physical model

The dynamics of the asteroid and the spacecraft are modeled using classical rigid body dynamic equations, considering gravitational attraction from the Sun. The reduced timespan of the simulation allows to neglect the perturbation effect due to the mutual gravitational attraction.

2.1 Reference frames

Three reference frames are used to describe the position and velocity of the asteroid and the spacecraft: the heliocentric ecliptic coordinate system, the Hill's frame and the spacecraft's body fixed frame.

2.1.1 Heliocentric ecliptic coordinate system

The heliocentric ecliptic coordinate system, denoted as E and with unit vectors $(\hat{\boldsymbol{\imath}}, \hat{\boldsymbol{\jmath}}, \hat{\boldsymbol{k}})$, has origin at the center of the Sun, its fundamental plane is the ecliptic plane and the $\hat{\boldsymbol{\imath}}$ axis points towards the vernal point. It is right handed and inertial.

2.1.2 Hill's rotating frame

Considering the position of the asteroid with respect to the Sun $\boldsymbol{r}_a$, its velocity $\dot{\boldsymbol{r}}_a$ and its specific angular momentum $\boldsymbol{h} = \boldsymbol{r}_a \times \dot{\boldsymbol{r}}_a$, the axes of the Hill's frame are defined as

$$\hat{\boldsymbol{r}} = \boldsymbol{r}_a / \|\boldsymbol{r}_a\|, \quad \hat{\boldsymbol{\theta}} = \hat{\boldsymbol{h}} \times \hat{\boldsymbol{r}}, \quad \hat{\boldsymbol{h}} = \boldsymbol{h} / \|\boldsymbol{h}\|. \tag{1}$$

For the sake of simplicity in notation, $\hat{\boldsymbol{r}}$ indicates the unit vector of $\boldsymbol{r}_a$, even if the subscript a is omitted. The Hill's frame is centered in the asteroid's center of mass.

Since the asteroid is orbiting around the Sun with angular velocity $\boldsymbol{\omega}_a = \dot{\theta}\,\hat{\boldsymbol{h}}$, where θ is the true anomaly, the unit vectors $\hat{\boldsymbol{r}}$ and $\hat{\boldsymbol{\theta}}$ are time dependent; their time derivatives are:

$$\begin{cases} \dot{\hat{\boldsymbol{r}}} = \boldsymbol{\omega} \times \hat{\boldsymbol{r}} = \dot{\theta}\,\hat{\boldsymbol{\theta}} \\ \dot{\hat{\boldsymbol{\theta}}} = \boldsymbol{\omega} \times \hat{\boldsymbol{\theta}} = -\dot{\theta}\,\hat{\boldsymbol{r}} \end{cases} ; \quad \begin{cases} \ddot{\hat{\boldsymbol{r}}} = \ddot{\theta}\,\hat{\boldsymbol{\theta}} + \boldsymbol{\omega} \times (\dot{\theta}\,\hat{\boldsymbol{\theta}}) = \ddot{\theta}\,\hat{\boldsymbol{\theta}} - \dot{\theta}^2\,\hat{\boldsymbol{r}} \\ \ddot{\hat{\boldsymbol{\theta}}} = -\ddot{\theta}\,\hat{\boldsymbol{r}} + \boldsymbol{\omega} \times (-\dot{\theta}\,\hat{\boldsymbol{r}}) = -\ddot{\theta}\,\hat{\boldsymbol{r}} - \dot{\theta}^2\,\hat{\boldsymbol{\theta}} \end{cases} \tag{2}$$

2.1.3 Body fixed frame

The body fixed frame is fixed on the spacecraft and is composed of its principal axes of inertia. It will be denoted by the letter B and the unit vectors $(\hat{\boldsymbol{x}}, \hat{\boldsymbol{y}}, \hat{\boldsymbol{z}})$. Since the spacecraft attitude is not constant, this frame is not inertial.

The attitude of the spacecraft with respect to the ecliptic frame is represented using quaternions [4], implemented as column vectors:

$$\boldsymbol{q} = q_w + q_x \boldsymbol{i} + q_y \boldsymbol{j} + q_z \boldsymbol{k}, \qquad \boldsymbol{q} = \begin{bmatrix} q_w & q_x & q_y & q_z \end{bmatrix}^T \tag{3}$$

For a rotation θ around a unit vector (u_x, u_y, u_z), the quaternion will be:

$$\boldsymbol{q} = \cos(\theta/2) + (u_x \boldsymbol{i} + u_y \boldsymbol{j} + u_z \boldsymbol{k}) \sin(\theta/2) \tag{4}$$

A vector $\boldsymbol{v}$ can be rotated using the Hamilton product $\times$:

$$\begin{bmatrix} 0 \\ \boldsymbol{v}^B \end{bmatrix} = \boldsymbol{q}^* \times \begin{bmatrix} 0 \\ \boldsymbol{v}^E \end{bmatrix} \times \boldsymbol{q} \tag{5}$$

The rotation matrix to convert a vector from the ecliptic frame to the body fixed frame can be obtained from the rotation quaternion as

$$\mathbf{A}_{B/E} = \begin{bmatrix} q_{\mathtt{w}}^2 + q_{\mathtt{x}}^2 - q_{\mathtt{y}}^2 - q_{\mathtt{z}}^2 & 2(q_{\mathtt{x}} q_{\mathtt{y}} + q_{\mathtt{w}} q_{\mathtt{z}}) & 2(q_{\mathtt{x}} q_{\mathtt{z}} - q_{\mathtt{w}} q_{\mathtt{y}}) \\ 2(q_{\mathtt{x}} q_{\mathtt{y}} - q_{\mathtt{w}} q_{\mathtt{z}}) & q_{\mathtt{w}}^2 - q_{\mathtt{x}}^2 + q_{\mathtt{y}}^2 - q_{\mathtt{z}}^2 & 2(q_{\mathtt{y}} q_{\mathtt{z}} + q_{\mathtt{w}} q_{\mathtt{x}}) \\ 2(q_{\mathtt{x}} q_{\mathtt{z}} + q_{\mathtt{w}} q_{\mathtt{y}}) & 2(q_{\mathtt{y}} q_{\mathtt{z}} - q_{\mathtt{w}} q_{\mathtt{x}}) & q_{\mathtt{w}}^2 - q_{\mathtt{x}}^2 - q_{\mathtt{y}}^2 + q_{\mathtt{z}}^2 \end{bmatrix} \tag{6}$$

2.2 Asteroid translational dynamics

The asteroid is assumed to be subjected only to Sun's gravity: the other perturbing forces are assumed to have negligible effects in the short timespan of the simulation. Consequently, the asteroid is on a Keplerian orbit and its motion can be described using its true anomaly θ. The dynamical equations can be derived from Newton's gravitation law:

$$\ddot{\boldsymbol{r}}_{\boldsymbol{a}} = -\frac{\mu}{r_a^3} \boldsymbol{r}_a = -\frac{\mu}{r_a^2} \hat{\boldsymbol{r}} \tag{7}$$

where μ is the standard gravitational parameter of the Sun and $\hat{\boldsymbol{r}} = \boldsymbol{r}_a / r_a$ as previously defined. The acceleration can be obtained by differentiating twice the position $\boldsymbol{r}_a$:

$$\ddot{\boldsymbol{r}}_a = \left(\ddot{r}_a - r_a \dot{\theta}^2 \right) \hat{\boldsymbol{r}} + \left(r_a \ddot{\theta} + 2 \dot{r}_a \dot{\theta} \right) \hat{\boldsymbol{\theta}} \tag{8}$$

Substituting (8) into (7), and considering that $\hat{\boldsymbol{r}}$ and $\hat{\boldsymbol{\theta}}$ are orthogonal, the system of coupled nonlinear ordinary differential equations that describe the orbit of the asteroid around the Sun is obtained:

$$\ddot{r}_a = r_a \, \dot{\theta}^2 - \frac{\mu}{r_a^2}; \qquad \ddot{\theta} = -2 \frac{\dot{r}_a}{r_a} \dot{\theta} \tag{9}$$

2.3 Spacecraft dynamics

The motion of the spacecraft is assumed to be governed by the Sun's gravitational force and the control force:

$$\ddot{\boldsymbol{r}}_s = -\frac{\mu}{r_s^3}\boldsymbol{r}_s + \frac{\boldsymbol{f}}{m_s} \tag{10}$$

where $\boldsymbol{r}_s$ is the position vector of the spacecraft with respect to the Sun, $\boldsymbol{f}$ is the control force and m_s is the mass of the spacecraft. The control force will be computed in the body frame, while the dynamic equations of the spacecraft will be written in the Hill's frame. The conversion from one frame to the other is achieved using the rotation matrix $\mathbf{A}_{H/B}$, which can be obtained from the matrices that relate the Hill's and the body frames to the ecliptic frame ($\mathbf{A}_{H/E}$ and $\mathbf{A}_{B/E}$, respectively):

$$\boldsymbol{f}^H = \begin{bmatrix} f_x & f_y & f_z \end{bmatrix}_H^T = \mathbf{A}_{H/B}\,\boldsymbol{f}^B, \quad \mathbf{A}_{H/B} = \mathbf{A}_{H/E}\,\mathbf{A}_{B/E}^T \tag{11}$$

It is convenient to use the relative position vector between the spacecraft and the asteroid:

$$\boldsymbol{\rho} = \boldsymbol{r}_s - \boldsymbol{r}_a = x\hat{\boldsymbol{r}} + y\hat{\boldsymbol{\theta}} + z\hat{\boldsymbol{h}} \tag{12}$$

Considering that the second derivative of $\boldsymbol{r}_s$ is $\ddot{\boldsymbol{r}}_s = \ddot{\boldsymbol{r}}_a + \ddot{\boldsymbol{\rho}}$ and using Eqs. (7) and (10), the relative translational dynamics can be obtained [12,5]:

$$\begin{cases} \ddot{x} - 2\dot{\theta}\dot{y} - \ddot{\theta}y - \dot{\theta}^2 x = -\mu\,(r+x)/r_s^3 + f_x/m_s + \mu/r_a^2 \\ \ddot{y} + 2\dot{\theta}\dot{x} + \ddot{\theta}x - \dot{\theta}^2 y = -\mu\,(\quad y\quad)/r_s^3 + f_y/m_s \\ \ddot{z} = -\mu\,(\quad z\quad)/r_s^3 + f_z/m_s \end{cases} \tag{13}$$

The attitude is governed by Euler's rotation equation and by quaternion kinematics [4]:

$$\mathbf{I}^B\dot{\boldsymbol{\omega}}^B + \boldsymbol{\omega}^B \times \left(\mathbf{I}^B\boldsymbol{\omega}^B\right) = \boldsymbol{m}^B; \quad \dot{\boldsymbol{q}} = \frac{1}{2}\begin{bmatrix} 0 \\ \boldsymbol{\omega}^B \end{bmatrix} \times \boldsymbol{q} \tag{14}$$

where $\boldsymbol{\omega}^B$ is the spacecraft angular velocity, $\mathbf{I}^B$ its inertia matrix, and $\boldsymbol{m}^B$ the applied torque.

3 Navigation

The relative attitude and position of the spacecraft with respect to the asteroid must be estimated to control the trajectory until impact. The measurements of a star tracker, a gyroscope and a navigation camera are used and processed with properly designed Kalman filters to reconstruct the state of the system.

3.1 Navigation camera

The image acquired by the navigation camera is simulated using the Blender® software, considering the relative position of the spacecraft with respect to the asteroid and the camera's optical properties. The image is then interpreted by a processing algorithm that returns the angular position of the asteroid in the FOV. These angles are then processed by the Kalman filter to estimate the translational state.

As reported in Fig. 1, the image is read into a matrix of 8-bit values (from 0 for black to 255 for white). A threshold filter is applied and a circle is fitted on the illuminated border of the asteroid. This gives an estimation of the center of the asteroid in the FOV. A more detailed description of these operations follows.

Fig. 1 Image analysis algorithm

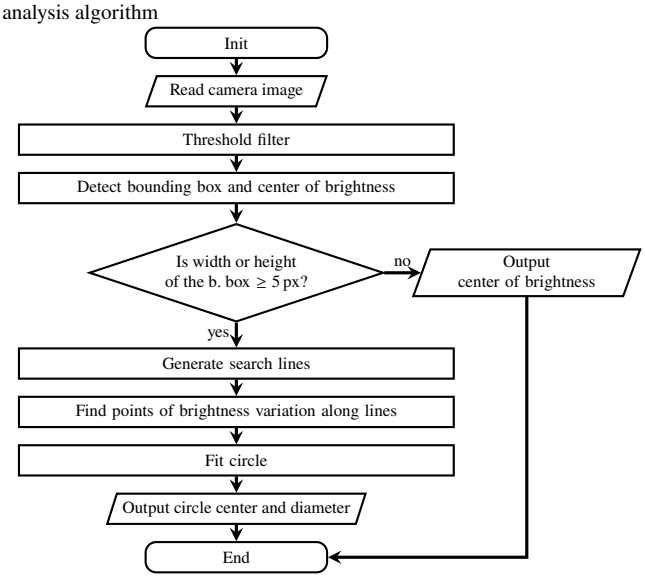

Brightness threshold. The pixels beyond a given brightness threshold are determined. This returns a boolean matrix, where the asteroid's image is formed by ones and the background is translated into zeros.

Bounding box and brightness centroiding. The matrix is scanned to find the smallest box that contains all the illuminated pixels to locate the asteroid in the image. A weighted mean of the position of the illuminated pixels gives the center of brightness (COB), which serves as a preliminary estimate of the asteroid center. With $\mathbf{B}$ the boolean matrix (true and false are 1 and 0, respectively), the COB can be computed as

$$\boldsymbol{CoB} = \left(\frac{\sum_{i,j} i\, \mathbf{B}(i,j)}{\sum_{i,j} \mathbf{B}(i,j)}, \frac{\sum_{i,j} j\, \mathbf{B}(i,j)}{\sum_{i,j} \mathbf{B}(i,j)} \right) \tag{15}$$

Circular fitting. A possible way to mitigate the error between the center of brightness and the center of mass is to guess the shape of the asteroid. When its image is large enough, it is possible to fit a circular shape using the illuminated points; then, the center of the circle is used instead of the COB. The determination of the points on the border is based on search lines parallel to the direction of the Sun rays, in order to use only the illuminated edge of the asteroid. The image analyzer computes the orientation of the search lines using the estimated spacecraft attitude and the nominal orbital position of the asteroid. The state covariance is not considered in this process.

The equation of a circle with radius r centered in (c_x, c_y) is:

$$x^2 + y^2 = 2\,c_x\,x + 2\,c_y\,y + r^2 - (c_x^2 + c_y^2) \tag{16}$$

This equation, applied to each fitting point (x_i, y_i), leads to the linear system:

$$\begin{bmatrix} x_1 & y_1 & 1 \\ \vdots & \vdots & \vdots \\ x_N & y_N & 1 \end{bmatrix} \mathbf{a} = \begin{bmatrix} x_1^2 + y_1^2 \\ \vdots \\ x_N^2 + y_N^2 \end{bmatrix}; \quad \text{with solution:} \quad \boldsymbol{a} = \begin{bmatrix} 2\,c_x \\ 2\,c_y \\ r^2 - (c_x^2 + c_y^2) \end{bmatrix} \tag{17}$$

With a least-squares approximation, it is possible to obtain $\boldsymbol{a}$, i.e. the parameters in Eq. (16). The resulting center and diameter are used to determine the position and the size of the asteroid, using optical relations that will be introduced afterwards.

Other shapes could be used, for instance elliptical fitting could ideally be more suitable for asteroids with elongated shape. In this case, the fitting parameters are the position of the center, the length of the axes and an orientation angle. However, in the frame of preliminary tests, elliptical fitting turned out to be less robust due to the concentration of the fitting points in the illuminated side of the asteroid. This is evident in Fig. 2 (left), where the obtained circle and ellipse are overlaid. The circle fits well the shape of the asteroid, while the resulting ellipse is twice the correct size, with a center almost outside of the asteroid. The adoption of elliptical shapes in the fitting process will be investigated further in future studies.

The algorithms have also been tested on asteroid Itokawa (Fig. 2, right): both the circular and the elliptical fits give a smaller estimation of the size of the asteroid, leading to an estimation of the center that shifts towards the illuminated border.

Fig. 2 Different fitting methods applied to Bennu and Itokawa (straight lines = scan lines, magenta circles = detected fitting points, green dashed line = reference circle with 550 m diameter, red line = fitted circle, light blue line = fitted ellipse, black $*$ = center of brightness (COB))

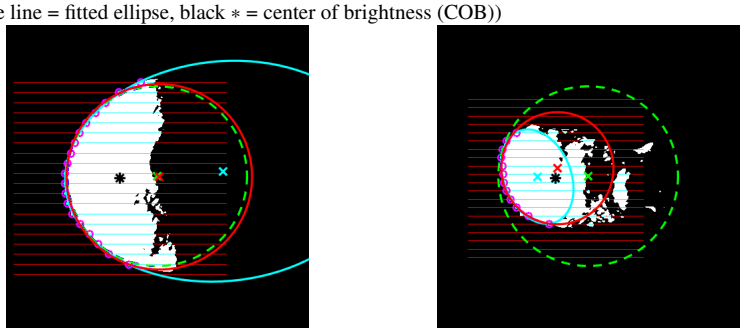

3.1.1 Optical properties and relations

The mathematical relations to convert the position of the asteroid in the image to the measurement processed by the Kalman filter are reported below.

Focal Length. Assuming that the asteroid distance is much longer than the size of the camera, the Focal Length (FL) is the distance between the sensor and the lens.

Field Of View. The Field Of View (FOV) is the solid angle detected by the camera.

Resolution. The resolution (Res) is the number of pixels on the sensor of the camera, that is supposed to be square (in size and resolution).

Size of the sensor. The length of its sides can be obtained from the relation:

$$\text{SensorSideLength} = 2 \times \text{FL} \times \tan\left(\text{FOV}/2\right) \tag{18}$$

The meaning of this equation is that, in order to obtain a longer FL while keeping the same FOV, the sensor must be enlarged proportionally; otherwise, the FOV is reduced.

Size of a pixel. Since the sensor is a uniform grid composed by Res-by-Res pixels, each of them is a square with sides of length:

$$\text{PixelSideLength} = \text{SensorSideLength}/\text{Res} \tag{19}$$

Angular measurements. The image is stored in terms of a square matrix of size Res-by-Res. The following procedure is adopted to retrieve the physical position of a pixel, in terms of the azimuth and elevation angles. First, the index range is centered:

$$[1; \text{Res}] \rightarrow [-(\text{Res}-1)/2; +(\text{Res}-1)/2] \tag{20}$$

Then, a Cartesian coordinate centered on the sensor can be obtained by multiplying the range in Eq. (20) by the size of a pixel. The ratio of the position on the sensor with respect to the focal length represents the tangent of the angle in the camera FOV, which will be considered equal to the angle itself. The overall formula to convert the position of a pixel (PixelPos) in the range $[1; \text{Res}]$ to a camera angle is:

$$\text{CameraAngles} = (\text{PixelPos} - 0.5\,\text{px} - \text{Res}/2) \times \text{PixelSideLength}/\text{FL} \tag{21}$$

Image size. Since the diameter of the asteroid and its projection on the sensor form, with the lens, two triangles in similarity relationship, it is possible to convert the physical size (AstDiameter) to the projected size on the sensor (AstImgDiameter):

$$\text{AstImgDiameter} = \text{AstDiameter} \times \text{FL}/\text{Distance} \tag{22}$$

The size in pixels ($\text{AstImgDiameter}_{\text{Px}}$) can be computed by dividing the physical size of the image on the sensor by the size of a pixel:

$$\text{AstImgDiameter}_{\text{Px}} = \frac{\text{AstImgDiameter}}{\text{PixelSideLength}} = \frac{\text{AstImgDiameter} \times \text{Res}}{\text{SensorSideLength}} \tag{23}$$

3.2 Filtering

The implemented feedback control acts on the state of the system, yet the spacecraft does not have direct measurements of it. In order to obtain sufficiently accurate estimates of the spacecraft state, the measurements given by the sensors are processed by a Kalman filter. Kalman filters need the state space equations and the measurements of the system:

$$\dot{\boldsymbol{x}}(t) = \boldsymbol{f}\left(\boldsymbol{x}(t)\right) + \boldsymbol{u}(t); \quad \tilde{\boldsymbol{y}}(t) = \boldsymbol{h}\left(\boldsymbol{x}(t), t\right) + \boldsymbol{v}(t) \quad \boldsymbol{v}(t) \sim \mathcal{N}\left(\mathbf{0}, \mathbf{R}(t)\right) \tag{24}$$

where $\boldsymbol{x}$ is the state vector, $\boldsymbol{u}$ is the input (the control action) and $\tilde{\boldsymbol{y}}$ is the measurement from the sensor with additive noise $\boldsymbol{v}$; $\boldsymbol{f}$ and $\boldsymbol{h}$ are the state transition and observation functions, $\mathbf{R}$ is the observation noise covariance. The dynamics of the system have been assumed to be affine in the control action.

Extended Kalman filters need also a linearized version of the equations:

$$\dot{\boldsymbol{x}}(t) = \mathbf{F}(t)\boldsymbol{x}(t) + \boldsymbol{u}(t); \quad \tilde{\boldsymbol{y}}(t) = \mathbf{H}(t)\boldsymbol{x}(t) + \boldsymbol{v}(t) \quad \boldsymbol{v}(t) \sim \mathcal{N}\left(\mathbf{0}, \mathbf{R}(t)\right) \tag{25}$$

where $\mathbf{F}$ and $\mathbf{H}$ are the Jacobian matrices of $\boldsymbol{f}$ and $\boldsymbol{h}$ with respect to the state.

3.2.1 Translation state equations

The translational state of the system includes the position and velocity of the spacecraft with respect to the asteroid written in the Hill's reference frame $\boldsymbol{\rho}$:

$$\boldsymbol{x} = \begin{bmatrix} \boldsymbol{\rho} \\ \dot{\boldsymbol{\rho}} \end{bmatrix}, \quad \dot{\boldsymbol{x}} = \begin{bmatrix} \dot{\boldsymbol{\rho}} \\ \ddot{\boldsymbol{\rho}} \end{bmatrix}; \quad \mathbf{F} = \frac{\partial \dot{\boldsymbol{x}}}{\partial \boldsymbol{x}} = \begin{bmatrix} \frac{\partial \dot{\boldsymbol{\rho}}}{\partial \boldsymbol{\rho}} & \frac{\partial \dot{\boldsymbol{\rho}}}{\partial \dot{\boldsymbol{\rho}}} \\ \frac{\partial \ddot{\boldsymbol{\rho}}}{\partial \boldsymbol{\rho}} & \frac{\partial \ddot{\boldsymbol{\rho}}}{\partial \dot{\boldsymbol{\rho}}} \end{bmatrix} \tag{26}$$

Considering that the state affects also $\boldsymbol{r}_s$ since $\boldsymbol{r}_s = \boldsymbol{r}_a + \boldsymbol{\rho}$, the Jacobian is:

$$\frac{\partial \dot{\boldsymbol{\rho}}}{\partial \boldsymbol{\rho}} = \mathbf{0}_3, \; \frac{\partial \dot{\boldsymbol{\rho}}}{\partial \dot{\boldsymbol{\rho}}} = \mathbf{I}_3, \; \frac{\partial \ddot{\boldsymbol{\rho}}}{\partial \boldsymbol{\rho}} = \begin{bmatrix} \dot{\theta}^2 & \ddot{\theta} & 0 \\ -\ddot{\theta} & \dot{\theta}^2 & 0 \\ 0 & 0 & 0 \end{bmatrix} - \frac{\mu}{r_s^3}\mathbf{I}_3 + 3\frac{\mu}{r_s^5}\left[\boldsymbol{r}_s \boldsymbol{r}_s^T\right], \; \frac{\partial \ddot{\boldsymbol{\rho}}}{\partial \dot{\boldsymbol{\rho}}} = \begin{bmatrix} 0 & 2\dot{\theta} & 0 \\ -2\dot{\theta} & 0 & 0 \\ 0 & 0 & 0 \end{bmatrix} \tag{27}$$

The measurements given by the camera are the azimuth and elevation of the asteroid in the FOV; using the previously presented optical relations, they can be computed as:

$$\boldsymbol{h} = \begin{bmatrix} \gamma & \alpha \end{bmatrix}^T = \begin{bmatrix} -a/c & +b/c \end{bmatrix}^T \tag{28}$$

where (a, b, c) is Line Of Sight (LOS) unit vector in the body frame:

$$\hat{\boldsymbol{\rho}}^B = \begin{bmatrix} a & b & c \end{bmatrix}_B^T = \boldsymbol{\rho}^B/\rho = \mathbf{A}_{B/H}\boldsymbol{\rho}^H/\rho = \mathbf{A}_{B/H}\hat{\boldsymbol{\rho}}^H \tag{29}$$

The measurement equation can now be expressed as:

$$\boldsymbol{h} = \boldsymbol{h}(\hat{\boldsymbol{\rho}}^B) = \boldsymbol{h}(\mathbf{A}_{B/H}(\boldsymbol{q})\boldsymbol{\rho}^H/\rho) \tag{30}$$

It is now necessary to compute the Jacobian matrix of the measurement function with respect to the state of the system:

$$\mathbf{H} = \frac{\partial \boldsymbol{h}}{\partial \boldsymbol{\rho}^H} = \frac{\partial \boldsymbol{h}}{\partial \hat{\boldsymbol{\rho}}^B} \frac{\partial \hat{\boldsymbol{\rho}}^B}{\partial \hat{\boldsymbol{\rho}}^H} \frac{\partial \hat{\boldsymbol{\rho}}^H}{\partial \boldsymbol{\rho}^H} \tag{31}$$

$$\frac{\partial \boldsymbol{h}}{\partial \hat{\boldsymbol{\rho}}^B} = \begin{bmatrix} -1/c & 0 & a/c^2 \\ 0 & 1/c & -b/c^2 \end{bmatrix}, \quad \frac{\partial \hat{\boldsymbol{\rho}}^B}{\partial \hat{\boldsymbol{\rho}}^H} = \mathbf{A}_{B/H} \tag{32}$$

$$\frac{\partial \hat{\boldsymbol{\rho}}}{\partial \boldsymbol{\rho}} = \frac{\partial \left(\boldsymbol{\rho} / \sqrt{\boldsymbol{\rho}^T \boldsymbol{\rho}} \right)}{\partial \boldsymbol{\rho}} = \frac{\mathbf{I}_3 \sqrt{\boldsymbol{\rho}^T \boldsymbol{\rho}} - \boldsymbol{\rho} \boldsymbol{\rho}^T / \sqrt{\boldsymbol{\rho}^T \boldsymbol{\rho}}}{\boldsymbol{\rho}^T \boldsymbol{\rho}} = \frac{\rho^2 \mathbf{I}_3 - \boldsymbol{\rho} \boldsymbol{\rho}^T}{\rho^3} \tag{33}$$

The derivatives of the measurement with respect to the rotation quaternion are:

$$\frac{\partial \boldsymbol{h}}{\partial \boldsymbol{q}} = \frac{\partial \boldsymbol{h}}{\partial \hat{\boldsymbol{\rho}}^B} \left[\frac{\partial \mathbf{A}_{B/H}}{\partial q_{\mathtt{w}}} \hat{\boldsymbol{\rho}}^H \ \frac{\partial \mathbf{A}_{B/H}}{\partial q_{\mathtt{x}}} \hat{\boldsymbol{\rho}}^H \ \frac{\partial \mathbf{A}_{B/H}}{\partial q_{\mathtt{y}}} \hat{\boldsymbol{\rho}}^H \ \frac{\partial \mathbf{A}_{B/H}}{\partial q_{\mathtt{z}}} \hat{\boldsymbol{\rho}}^H \right] \tag{34}$$

The derivatives of $\mathbf{A}_{B/H}$ can be derived considering Eq. (6).

The estimated attitude of the spacecraft (Sec. 3.2.2) is expressed as a rotation between the body frame and the inertial frame ($\boldsymbol{q}_{B/E}$), while the quaternion in Eq. (34) is between body frame and Hill's frame ($\boldsymbol{q}_{B/H}$). Therefore it is necessary to convert the rotation and its covariance $\boldsymbol{\Sigma}$:

$$\boldsymbol{q}_{B/E} = \boldsymbol{q}_{B/H} \times \boldsymbol{q}_{H/E} \quad \Longrightarrow \quad \boldsymbol{q}_{B/E} = \boldsymbol{q}_{B/E} \times \boldsymbol{q}^*_{H/E} \tag{35}$$

$$\boldsymbol{\Sigma}_{\boldsymbol{q}_{B/H}} = \mathbf{J}_{\boldsymbol{q}} \, \boldsymbol{\Sigma}_{\boldsymbol{q}_{B/H}} \, \mathbf{J}_{\boldsymbol{q}}^T; \quad \mathbf{J}_q = \frac{\partial \left(\boldsymbol{q}_{B/E} \times \boldsymbol{q}^*_{H/E} \right)}{\partial \boldsymbol{q}_{H/E}} = \begin{bmatrix} +q_{\mathtt{w}} & +q_{\mathtt{x}} & +q_{\mathtt{y}} & +q_{\mathtt{z}} \\ -q_{\mathtt{x}} & +q_{\mathtt{w}} & -q_{\mathtt{z}} & +q_{\mathtt{y}} \\ -q_{\mathtt{y}} & +q_{\mathtt{z}} & +q_{\mathtt{w}} & -q_{\mathtt{x}} \\ -q_{\mathtt{z}} & -q_{\mathtt{y}} & +q_{\mathtt{x}} & +q_{\mathtt{w}} \end{bmatrix} \tag{36}$$

3.2.2 Rotation state equations

The state of the system for the rotational dynamics is composed of its angular velocity $\boldsymbol{\omega}^B$ and its attitude quaternion $\boldsymbol{q}_{B/E}$ (with respect to the inertial reference frame):

$$\boldsymbol{x} = \begin{bmatrix} \boldsymbol{\omega} \\ \boldsymbol{q} \end{bmatrix}, \quad \dot{\boldsymbol{x}} = \begin{bmatrix} \dot{\boldsymbol{\omega}} \\ \dot{\boldsymbol{q}} \end{bmatrix}; \quad \mathbf{F} = \frac{\partial \dot{\boldsymbol{x}}}{\partial \boldsymbol{x}} = \begin{bmatrix} \frac{\partial \dot{\boldsymbol{\omega}}}{\partial \boldsymbol{\omega}} & \frac{\partial \dot{\boldsymbol{\omega}}}{\partial \boldsymbol{q}} \\ \frac{\partial \dot{\boldsymbol{q}}}{\partial \boldsymbol{\omega}} & \frac{\partial \dot{\boldsymbol{q}}}{\partial \boldsymbol{q}} \end{bmatrix} \tag{37}$$

The superscript ^{B} and the subscript $_{B/E}$ are omitted to simplify the notation. The Jacobian can be obtained from the rotational equations (14).

The rotational state estimation relies on the measurements provided by a star tracker and a gyroscope. The corresponding necessary relations are reported hereafter.

Star tracker. Star trackers acquire images of deep space in order to reconstruct the attitude of the spacecraft using the position of the stars in their FOV. Within this work, the star tracker provides directly angular measurements of the spacecraft attitude. Choosing for example the Tait-Bryan angles, which describe the rotations as $\mathbf{Q}_z(\psi)\mathbf{Q}_y(\theta)\mathbf{Q}_x(\phi)$ ([1, p. 39], with $\mathbf{Q}_i(\alpha)$: rotation matrix of angle α about the i axis), the measurement function and its Jacobian are:

$$\boldsymbol{h} = \begin{bmatrix}\phi\\ \theta\\ \psi\end{bmatrix} = \begin{bmatrix}\text{atan2}\,(a_1, a_2)\\ \text{asin}\,(a_3)\\ \text{atan2}\,(a_4, a_5)\end{bmatrix} \quad \text{with}: \quad \begin{cases} a_1 = q_\mathtt{w}\, q_\mathtt{x} + q_\mathtt{y}\, q_\mathtt{z} \\ a_2 = 1/2 - (q_\mathtt{x}^2 + q_\mathtt{y}^2) \\ a_3 = 2\,(q_\mathtt{w}\, q_\mathtt{y} - q_\mathtt{z}\, q_\mathtt{x}) \\ a_4 = q_\mathtt{w}\, q_\mathtt{z} + q_\mathtt{x}\, q_\mathtt{y} \\ a_5 = 1/2 - (q_\mathtt{y}^2 + q_\mathtt{z}^2) \end{cases} \tag{38}$$
$$\mathbf{H} = \frac{\partial \boldsymbol{h}}{\partial \boldsymbol{x}} = \begin{bmatrix}\mathbf{0}_3 & \dfrac{\partial \boldsymbol{h}}{\partial \boldsymbol{q}}\end{bmatrix}$$

Gyroscope. The gyroscope measurement function and the corresponding Jacobian are:

$$\boldsymbol{h} = \boldsymbol{\omega}^B; \quad \mathbf{H} = \frac{\partial \boldsymbol{h}}{\partial \boldsymbol{x}} = \begin{bmatrix}\mathbf{I}_3 & \mathbf{0}_{3,4}\end{bmatrix} \tag{39}$$

3.2.3 Consider Extended Kalman filter equations

The reconstruction of the state is performed using a continuous-discrete Consider Extended Kalman Filter (CEKF) [13]. The CEKF is an extension of the EKF that accounts for the effect of a bias in the estimation directly in the propagated covariance matrix. In this way, it is possible to take into consideration that the center of mass of the asteroid may not coincide with the center identified in the image. This can be modeled as a displacement $\bar{\boldsymbol{\rho}}$ added to the estimated position $\tilde{\boldsymbol{\rho}}$:

$$\boldsymbol{\rho}(t) = \tilde{\boldsymbol{\rho}}(t) + \bar{\boldsymbol{\rho}}, \quad \boldsymbol{\rho}^H = \begin{bmatrix}x & y & z\end{bmatrix}^T, \quad \tilde{\boldsymbol{\rho}}^H = \begin{bmatrix}\tilde{x} & \tilde{y} & \tilde{z}\end{bmatrix}^T, \quad \bar{\boldsymbol{\rho}}^H = \begin{bmatrix}\bar{x} & \bar{y} & \bar{z}\end{bmatrix}^T \tag{40}$$

The term $\bar{\boldsymbol{\rho}}$ is modeled as a Gaussian zero-mean random error. Considering Eq. (40), the previously derived system (13) becomes:

$$\begin{cases} \ddot{x} - 2\dot{\theta}\dot{y} - \ddot{\theta}(\tilde{y} + \bar{y}) - \dot{\theta}^2(\tilde{x} + \bar{x}) = -\mu\,(r + \tilde{x} + \bar{x})/r_s^3 + f_x/m_{SC} + \mu/r_c^2 \\ \ddot{y} + 2\dot{\theta}\dot{x} + \ddot{\theta}(\tilde{x} + \bar{x}) - \dot{\theta}^2(\tilde{y} + \bar{y}) = -\mu\,(\quad \tilde{y} + \bar{y} \quad)/r_s^3 + f_y/m_{SC} \\ \ddot{z} = -\mu\,(\quad \tilde{z} + \bar{z} \quad)/r_s^3 + f_z/m_{SC} \end{cases} \tag{41}$$

with $r_s = \left[(r_a + \tilde{x} + \bar{x})^2 + (\tilde{y} + \bar{y})^2 + (\tilde{z} + \bar{z})^2\right]^{1/2}$.

Therefore, the state to be estimated is:

$$\boldsymbol{x} = \begin{bmatrix}\tilde{\boldsymbol{\rho}} & \dot{\tilde{\boldsymbol{\rho}}}\end{bmatrix}^T, \quad \dot{\boldsymbol{x}} = \begin{bmatrix}\dot{\tilde{\boldsymbol{\rho}}} & \ddot{\tilde{\boldsymbol{\rho}}}\end{bmatrix}^T; \quad \dot{\boldsymbol{x}}(t) = \boldsymbol{f}\,(\boldsymbol{x}(t), \bar{\boldsymbol{\rho}}, t) + \boldsymbol{u}(t). \tag{42}$$

State propagation is not affected by the introduction of $\bar{\boldsymbol{\rho}}$, since its estimate is zero. The Jacobian $\mathbf{F}$ remains as previously derived and $\mathbf{B}_{\bar{\rho}}$, the Jacobian with respect to the displacement $\bar{\boldsymbol{\rho}}$, is the left half of $\mathbf{F}$ from Eq. (26), since the partial derivatives of a function of $\boldsymbol{\rho}$ with respect to $\boldsymbol{\rho}$, $\tilde{\boldsymbol{\rho}}$ or $\bar{\boldsymbol{\rho}}$, are identical:

$$\frac{\partial f(\boldsymbol{\rho})}{\partial \tilde{\boldsymbol{\rho}}} = \frac{\partial f(\boldsymbol{\rho})}{\partial \boldsymbol{\rho}}\frac{\partial \boldsymbol{\rho}}{\partial \tilde{\boldsymbol{\rho}}} = \frac{\partial f(\boldsymbol{\rho})}{\partial \boldsymbol{\rho}}, \quad \frac{\partial f(\boldsymbol{\rho})}{\partial \bar{\boldsymbol{\rho}}} = \frac{\partial f(\boldsymbol{\rho})}{\partial \boldsymbol{\rho}}\frac{\partial \boldsymbol{\rho}}{\partial \bar{\boldsymbol{\rho}}} = \frac{\partial f(\boldsymbol{\rho})}{\partial \boldsymbol{\rho}} \tag{43}$$

Table 1 Consider Extended Kalman Filter equations

Model	$\dot{\boldsymbol{x}}(t) = \boldsymbol{f}\ (\boldsymbol{x}(t), \bar{\boldsymbol{\rho}}, t) + \boldsymbol{u}(t); \quad \tilde{\boldsymbol{y}}(t) = \boldsymbol{h}(\boldsymbol{x}(t), \bar{\boldsymbol{\rho}}, t) + \boldsymbol{v}(t); \quad \boldsymbol{v}(t) \sim \mathcal{N}(\mathbf{0}, \mathbf{R}(t))$
Gain	$\mathbf{K} = \left(\mathbf{P}^-_{\boldsymbol{xx}}\mathbf{H}^T_{\boldsymbol{x}} + \mathbf{P}^-_{\boldsymbol{x}\bar{\boldsymbol{\rho}}}\mathbf{H}^T_{\bar{\boldsymbol{\rho}}}\right) \cdot$ $\cdot \left(\mathbf{H}_{\boldsymbol{x}}\mathbf{P}^-_{\boldsymbol{xx}}\mathbf{H}^T_{\boldsymbol{x}} + \mathbf{H}_{\boldsymbol{x}}\mathbf{P}^-_{\boldsymbol{x}\bar{\boldsymbol{\rho}}}\mathbf{H}^T_{\bar{\boldsymbol{\rho}}} + \mathbf{H}_{\bar{\boldsymbol{\rho}}}\mathbf{P}^-_{\bar{\boldsymbol{\rho}}\boldsymbol{x}}\mathbf{H}^T_{\boldsymbol{x}} + \mathbf{H}_{\bar{\boldsymbol{\rho}}}\mathbf{P}^-_{\bar{\boldsymbol{\rho}}\bar{\boldsymbol{\rho}}}\mathbf{H}^T_{\bar{\boldsymbol{\rho}}} + \mathbf{R}\right)^{-1}$
Update	$\hat{\boldsymbol{x}}^+ = \hat{\boldsymbol{x}}^- + \mathbf{K}\left(\tilde{\boldsymbol{y}} - \mathbf{H}_{\boldsymbol{x}}\hat{\boldsymbol{x}}^- - \mathbf{H}_{\bar{\boldsymbol{\rho}}}\hat{\bar{\boldsymbol{\rho}}}\right)$ $\mathbf{P}^+_{\boldsymbol{xx}} = (\mathbf{I} - \mathbf{K}\mathbf{H}_{\boldsymbol{x}})\,\mathbf{P}^-_{\boldsymbol{xx}} - \mathbf{K}\mathbf{H}_{\bar{\boldsymbol{\rho}}}\mathbf{P}^-_{\bar{\boldsymbol{\rho}}\boldsymbol{x}}; \quad \mathbf{P}^+_{\boldsymbol{x}\bar{\boldsymbol{\rho}}} = (\mathbf{I} - \mathbf{K}\mathbf{H}_{\boldsymbol{x}})\,\mathbf{P}^-_{\boldsymbol{x}\bar{\boldsymbol{\rho}}} - \mathbf{K}\mathbf{H}_{\bar{\boldsymbol{\rho}}}\mathbf{P}_{\bar{\boldsymbol{\rho}}\bar{\boldsymbol{\rho}}}$
Prop.	$\dot{\hat{\boldsymbol{x}}}(t) = \boldsymbol{f}\ \left(\hat{\boldsymbol{x}}(t), \hat{\bar{\boldsymbol{\rho}}}(t)\right) + \boldsymbol{u}(t)$ $\dot{\boldsymbol{P}}_{\boldsymbol{xx}}(t) = \mathbf{F}(t)\mathbf{P}_{\boldsymbol{xx}}(t) + \mathbf{P}_{\boldsymbol{xx}}(t)\mathbf{F}^T(t) + \mathbf{P}_{\boldsymbol{x}\bar{\boldsymbol{\rho}}}(t)\mathbf{B}^T_{\bar{\boldsymbol{\rho}}}(t) + \mathbf{B}_{\bar{\boldsymbol{\rho}}}(t)\mathbf{P}_{\bar{\boldsymbol{\rho}}\boldsymbol{x}}(t)$ $\dot{\boldsymbol{P}}_{\boldsymbol{x}\bar{\boldsymbol{\rho}}}(t) = \mathbf{F}(t)\mathbf{P}_{\boldsymbol{x}\bar{\boldsymbol{\rho}}}(t) + \mathbf{B}_{\bar{\boldsymbol{\rho}}}(t)\mathbf{P}_{\bar{\boldsymbol{\rho}}\bar{\boldsymbol{\rho}}}$

The equations of the CEKF are reported in Table 1. The equations in the first row describe the evolution of the state of the real system $\boldsymbol{x}$ and the readings of the sensors, $\boldsymbol{u}$ is the control force and $\boldsymbol{v}$ is the measurement noise with zero mean and covariance $\mathbf{R}$. The estimated state is integrated in time, along with its covariance, through the equations in the last row. The variation of the state covariance $\mathbf{P}_{xx}$ depends on $\mathbf{H}$, the Jacobian of $\boldsymbol{h}$. When a measurement is obtained by the sensor, the state and the covariance are updated accordingly, using the equations in the third row. $\mathbf{H}_x$ is the Jacobian of the measurement $\boldsymbol{h}$ and $\mathbf{K}$ is computed through the *gain* equation. The superscript + indicates the updated values of the variables, while the − the predicted ones. The quantities peculiar to the consider version of the EKF are:

- the *consider variable*: $\bar{\boldsymbol{\rho}}$;
- the cross-covariance between $\bar{\boldsymbol{\rho}}$ and the state of the system: $\mathbf{P}_{\bar{\boldsymbol{\rho}}\boldsymbol{x}}$ ($\mathbf{P}_{\boldsymbol{x}\bar{\boldsymbol{\rho}}} = \mathbf{P}^T_{\bar{\boldsymbol{\rho}}\boldsymbol{x}}$);
- the covariance matrix of $\bar{\boldsymbol{\rho}}$: $\mathbf{P}_{\bar{\boldsymbol{\rho}}\bar{\boldsymbol{\rho}}}$;
- the Jacobian of $\boldsymbol{f}$ with respect to $\bar{\boldsymbol{\rho}}$: $\mathbf{B}_{\bar{\boldsymbol{\rho}}}$.

4 Translational control

A control strategy based on Zero Effort errors [9] has been adopted. The Zero Effort Miss (ZEM) and the Zero Effort Velocity (ZEV) are defined as the error in position and velocity at the final instant if no control is applied:

$$\boldsymbol{ZEM}(t) = \boldsymbol{\rho}_d - \boldsymbol{\rho}_f(t); \quad \boldsymbol{ZEV}(t) = \dot{\boldsymbol{\rho}}_d - \dot{\boldsymbol{\rho}}_f(t) \tag{44}$$

where $\boldsymbol{\rho}_d$ and $\dot{\boldsymbol{\rho}}_d$ are the desired final position and velocity, while $\boldsymbol{\rho}_f(t)$ and $\dot{\boldsymbol{\rho}}_f(t)$ are the ones obtained if no control is applied from time t onwards. $\boldsymbol{\rho}_f(t)$ and $\dot{\boldsymbol{\rho}}_f(t)$ are obtained by integrating the motion from the current time t up to the final time t_f:

$$\boldsymbol{\rho}_f = \boldsymbol{\rho} + (t_f - t)\dot{\boldsymbol{\rho}} + \iint_t^{t_f} \ddot{\boldsymbol{\rho}}(\tau)\mathrm{d}\tau^2; \qquad \dot{\boldsymbol{\rho}}_f = \dot{\boldsymbol{\rho}} + \int_t^{t_f} \ddot{\boldsymbol{\rho}}(\tau)\mathrm{d}\tau \tag{45}$$

The control acceleration proportional to the ZEM/ZEV can be written as:

$$\boldsymbol{a}(t) = k_M(t)\,\boldsymbol{ZEM}(t) + k_V(t)\,\boldsymbol{ZEV}(t) \tag{46}$$

k_M and k_V can be tuned to minimize the fuel consumption while guaranteeing the impact. This optimization, if both the desired position and velocity are defined, gives:

$$\boldsymbol{a}(t) = 6/t_{go}^2\, \boldsymbol{ZEM}(t) - 2/t_{go}\, \boldsymbol{ZEV}(t) \tag{47}$$

If no constraint on the final velocity is given, the fuel-optimized acceleration is:

$$\boldsymbol{a}(t) = 3/t_{go}^2\, \boldsymbol{ZEM}(t) \tag{48}$$

The final instant has been defined as the moment at which the spacecraft is no more approaching the asteroid and is moving further beyond it. This occurs when the scalar product of the position and the velocity changes sign from negative to positive.

The gain increases with time and goes to infinity at the final instant. Therefore, a lower boundary on the estimated t_{go} is applied to prevent this risk. Also, it is affected by uncertainty, since it is computed from the estimated state. An estimation of its variance can be obtained using the linearized uncertainty propagation formula, that can give a safer estimation of the gains, substituting t_{go} with $t_{go} - 3\sigma_{t_{go}}$:

$$\sigma_{t_{go}}^2 \approx \frac{\partial t_{go}}{\partial \boldsymbol{x}} \boldsymbol{\Sigma}_{\boldsymbol{x}} \left(\frac{\partial t_{go}}{\partial \boldsymbol{x}}\right)^T ; \quad \frac{\partial t_{go}}{\partial \boldsymbol{x}} = \left[\frac{\partial t_{go}}{\partial \boldsymbol{\rho}} \;\; \frac{\partial t_{go}}{\partial \dot{\boldsymbol{\rho}}}\right] = \left[-\frac{\dot{\boldsymbol{\rho}}^T}{\dot{\boldsymbol{\rho}}\cdot\dot{\boldsymbol{\rho}}} \;\; -\frac{\boldsymbol{\rho}^T}{\dot{\boldsymbol{\rho}}\cdot\dot{\boldsymbol{\rho}}} + 2\frac{\boldsymbol{\rho}\cdot\dot{\boldsymbol{\rho}}}{(\dot{\boldsymbol{\rho}}\cdot\dot{\boldsymbol{\rho}})^2}\dot{\boldsymbol{\rho}}\right] \tag{49}$$

In the mission scenario of this work, the impact velocity is not imposed: only the lateral error is of interest to reach and impact the asteroid. Accordingly a perpendicular ZEM/ZEV control strategy is adopted. More specifically, two new parameters to cancel the longitudinal errors are introduced [8]:

- Perpendicular ZEM ($\boldsymbol{ZEM}_\perp$): position error computed at the instant at which the spacecraft misses the asteroid, i.e. when the velocity is normal to the position.
- Perpendicular ZEV ($\boldsymbol{ZEV}_\perp$): velocity component normal to the position vector.

Fig. 3 Perpendicular ZEM/ZEV definition (A=asteroid, S=spacecraft)

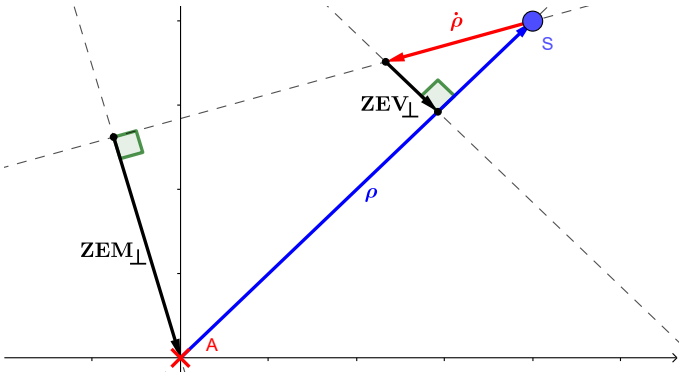

Neglecting the effects of the non-inertial frame, the motion with respect to the asteroid can be represented in a plane, as in Fig. 3, along with the newly introduced parameters. $\boldsymbol{ZEM}_\perp$ and $\boldsymbol{ZEV}_\perp$ can be computed as a function of the current state as:

$$\boldsymbol{ZEM}_\perp = (\boldsymbol{\rho}\cdot\hat{\dot{\boldsymbol{\rho}}})\hat{\dot{\boldsymbol{\rho}}} - \boldsymbol{\rho}\,; \quad \boldsymbol{ZEV}_\perp = (\dot{\boldsymbol{\rho}}\cdot\hat{\boldsymbol{\rho}})\hat{\boldsymbol{\rho}} - \dot{\boldsymbol{\rho}} \tag{50}$$

The control formulation will then use the same gains as in the standard ZEM and ZEV definition (the optimality of this decision has not been mathematically proved).

5 Attitude control

Attitude control is needed to point the navigation camera towards the asteroid. The camera is considered to be mounted on the -z axis of the spacecraft: the goal of the controller is to have $\hat{\boldsymbol{z}} = \hat{\boldsymbol{\rho}}$. The implemented control law is:

$$\boldsymbol{m}^B = -k_q \ \mathrm{sgn}\left(q_w^e\right) \ \left[q_x^e \ q_y^e \ q_z^e\right]^T - k_\omega \, \boldsymbol{\omega}^B \tag{51}$$

where $\boldsymbol{m}^B$ is the control torque, k_q and k_ω are tunable gains and $(q_w^e, q_x^e, q_y^e, q_z^e)$ is the error quaternion. The angular velocity is introduced to stabilize the spacecraft. This law is based on the property that the imaginary part of a quaternion represents the rotation axis. The sign of q_w^e accounts for the situation in which $\hat{\boldsymbol{z}}$ and $\hat{\boldsymbol{\rho}}$ are more than 90 deg apart. The error between $\hat{\boldsymbol{\rho}}$ and $\hat{\boldsymbol{z}}$ can be computed using its definition:

$$\boldsymbol{q}^e = \cos\left(\theta/2\right) + \hat{\boldsymbol{e}} \sin\left(\theta/2\right) \tag{52}$$

where $\hat{\boldsymbol{e}}$ is the axis of rotation and θ is the rotation angle, which can be computed as:

$$\hat{\boldsymbol{e}} = \left(\hat{\boldsymbol{\rho}} \times \hat{\boldsymbol{z}}\right) / \left\|\hat{\boldsymbol{\rho}} \times \hat{\boldsymbol{z}}\right\|, \quad \cos\theta = \hat{\boldsymbol{\rho}} \cdot \hat{\boldsymbol{z}}, \quad \sin\theta = \left\|\hat{\boldsymbol{\rho}} \times \hat{\boldsymbol{z}}\right\| \tag{53}$$

Using trigonometric relations, the control law in Eq. 51 becomes:

$$\boldsymbol{m}^B = -\left(k_q / \sqrt{2\left(1 + \hat{\boldsymbol{\rho}} \cdot \hat{\boldsymbol{z}}\right)}\right) \ \hat{\boldsymbol{\rho}}^B \times \hat{\boldsymbol{z}}^B - k_\omega \, \boldsymbol{\omega}^B \tag{54}$$

In the event that $\boldsymbol{\rho}$ and $\boldsymbol{z}$ are antiparallel, this gives an undefined result, and the error quaternion is built using an arbitrary unit vector normal to them for (q_x, q_y, q_z) and 0 for q_w. The gains have been chosen empirically as $k_q = 0.05$ and $k_\omega = 2$.

6 Simulation and results

A software tool has been devised and implemented to simulate the system and to validate the GNC strategy. Figure 4 illustrates the software architecture, with the interconnections of the modules of the simulator. The relative translational and rotational states derived from the integration of the equations of motion (which is referred to as true dynamics in the figure) are provided to Blender® for the generation of the simulated image. The image is then analysed to produce the associated measurement that is processed by the Kalman filter. The estimated state is used by the controller for the computation of the control action that is applied to the spacecraft. The dynamical model, the image analyzer, the Kalman filters and the actuators are implemented in MATLAB® and Simulink® (lower part of the figure), while the image of the camera is rendered using Blender® (upper part). The programs communicate through a Python interface.

Fig. 4 Simulator architecture

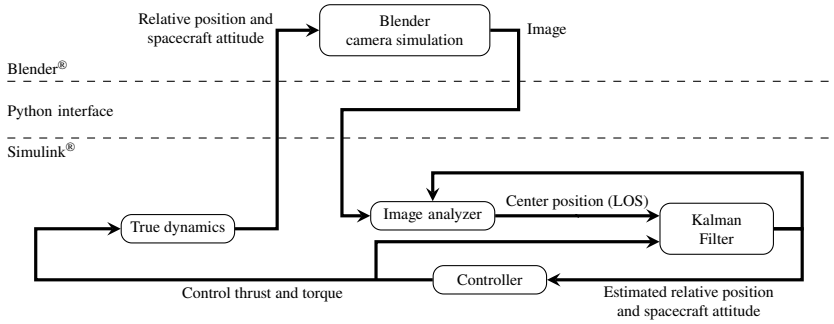

6.1 Simulation inputs

The position and velocity of the spacecraft and the orbital parameters of the asteroid at impact have been taken from Colombo et al. [3]. Table 2 reports the Keplerian elements of the asteroid at the impact instant. These elements provide the cartesian state reported in Table 3, expressed in the heliocentric ecliptic reference frame, along with the state of the spacecraft at the same instant.

a	1.055 923	AU
e	0.187 259	
i	0.015 892	rad
Ω	2.838 339	rad
ω	4.658 232	rad
θ	3.683 782	rad

Table 2 Asteroid Keplerian elements at impact

	Asteroid		Spacecraft	
x	0.223	AU	0.223	AU
y	−1.193	AU	−1.193	AU
z	0.017	AU	0.017	AU
$\dot{x}$	23.828	km/s	25.767	km/s
$\dot{y}$	7.353	km/s	8.386	km/s
$\dot{z}$	−0.225	km/s	−0.024	km/s

Table 3 Asteroid and spacecraft Cartesian state at impact

Figure 5 reports the orbits of the asteroid and the spacecraft before the impact, starting at 99 days before the impact (1/4 of the asteroid orbital period). The Sun-asteroid-spacecraft phase angle is approximately 73 deg.

Table 4 Initial conditions

Quantity	Nominal value	Error (1σ)
Position	From impact orbit	$10/3$ km
Velocity	From impact orbit	$1/3$ m/s
Ang. velocity	Zero	1×10^{-4} rad/s
Quaternion	Cam. pointing to ast.	1×10^{-4}

Fig. 5 Asteroid and spacecraft trajectories before impact

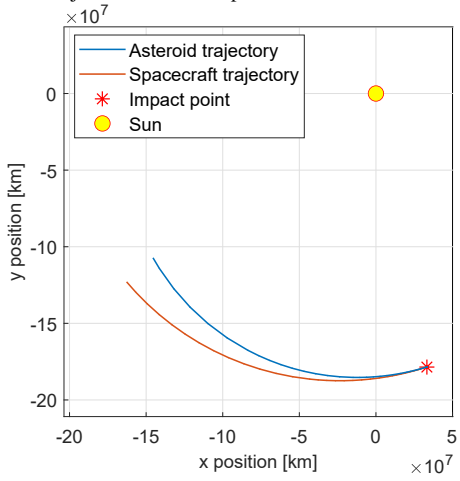

The initial data for the simulation have been obtained by backward propagation for 2000 s, starting from impact. The uncertainties applied to the initial conditions are reported in Table 4. These values are considered to be representative of the actual performance of a typical navigation system at the beginning of the simulated scenario. As a comparison, the Deep Impact mission expected a delivery error of 30 km ([10]).

The parameters used for the simulation are:

- spacecraft: mass 370 kg, moments of inertia 123.3x123.3x118.5 kgm^2
- camera: FL 152.5 mm, sensor size 13.3 mm 1944 px, FOV 5°, 1 image every 20 s;
- asteroid 3D model: 101955 Bennu (from NASA 3D Resources);
- image analysis algorithm: parallel lines, with max. 20 fitting points;
- 3σ center of mass bias: $1/3$ of the expected asteroid diameter (550 m).

The reference [3] proposed the use of the MSSS ECAM-C50 camera. Using the ECAM-C50, the asteroid image would be 1 px large from 3195 km and 5 px from 639 km. In order to gain better imaging performances, a telescopic camera has been considered in this work, with the requirement of detecting the asteroid as 1 px from 12 244 km and 5 px from 2449 km. Table 5 reports the relevant characteristics of the cameras and the attainable performance in this scenario (i.e. with a 550 m asteroid and a 2.2 km/s approach velocity). Figure 6 shows the asteroid image size as a function of

the distance and the corresponding time to impact for the two cameras. The selection of the most suitable reflectance model to render photorealistic images is left to future work. Therefore, no texture or reflectance model is set for the asteroid.

		ECAM-C50	**Proposed**
Focal Length	[mm]	12.6	152.5
Field Of View	[deg]	19	5
Resolution	[px]	1944	1944
Sensor size	[mm]	4.2	13.3
Pixel size	[µm]	2.2	6.9
Asteroid image size = 1 px			
Distance	[km]	3195	12 244
Time to impact	[s]	1452	5566
Asteroid image size = 5 px			
Distance	[km]	639	2449
Time to impact	[s]	290	1113
Asteroid image size = 1944 px (full size)			
Distance	[km]	2	6
Time to impact	[s]	1	3

Table 5 Considered cameras characteristics and attainable results

Fig. 6 Asteroid image size with respect to the distance for different cameras

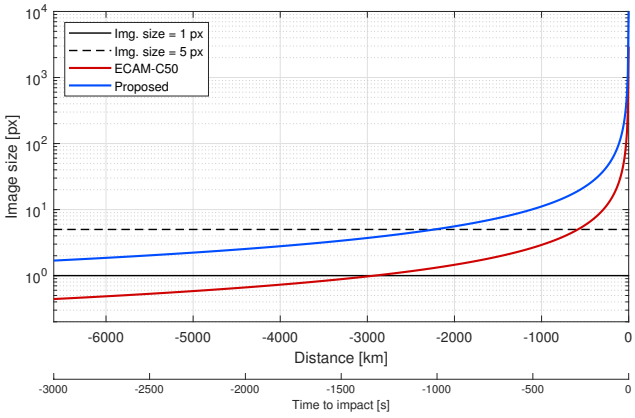

6.1.1 Modeling of sensors and actuators

The variance of the measurement of the center of the asteroid has been estimated with a Monte Carlo analysis using the almost spherical asteroid Bennu. The distance

Table 6 Sensor properties

Sensor	Error (1σ)	Rate
Camera angles	Variable (Eq. 56)	1/20 Hz
Star tracker	1×10^{-4} rad	1/5 Hz
Gyroscope	0.1 °/s	1/5 Hz

Table 7 Actuator assumptions

Property	Value for thrust	Value for torque
Delay	5 s	0.1 s
Control frequency	0.2 Hz	10 Hz
Saturation limit	5 N	1 mN m
Control level quantization	0.5 N	0.01 mN m
Transient rate limit between control levels	0.5 N/s	1 mNm/s

between the estimated and the true centers has been correlated to the asteroid image size obtained by the image processing algorithm. This has shown that the estimation error is proportional to the size of the asteroid, with a ratio around 5%:

$$3\sigma[\text{PixelPos}_{\text{center}}] = 5\% \times \text{ImageSizePx} \tag{55}$$

which means that the 3σ error on the estimation of the asteroid center in the image is 5% of its size (in pixels). Using the optical relations that convert the pixels position in the image to angles, the variance of azimuth and elevation can be obtained as:

$$\sigma^2[\text{CameraAngle}] = (5\% \times \text{AstImgSize}/3 \times \text{PixelSize}/\text{FocalLength})^2 \tag{56}$$

The parameters for all the sensors are reported in Table 6. The errors are applied on each component of the quantity (i.e. coordinate, angle or quaternion component).

The spacecraft is considered to be equipped with thrusters and reaction wheels. A simplified actuator model has been implemented, where the required thrust and torque are subjected to limitations, as reported in Table 7.

6.2 Results

Before presenting the results of the Monte Carlo analysis, a single run is executed to test the performance of the elements of the simulator, including the proposed GNC strategy. The initial realization of the state vector is set to its nominal value perturbed by an offset of $+1\sigma$ on each component. Figure 7 shows some example images acquired during the simulation. The labels report the time and distance to impact and the asteroid image diameter. The crosses represent the CoB (blue), the center of the fitted circle (yellow), the true center of the asteroid (green), and the target point as reconstructed by the filter (red). The search lines for the fitting points are reported in red and the obtained circle is white.

Fig. 7 Example images acquired during a simulation.

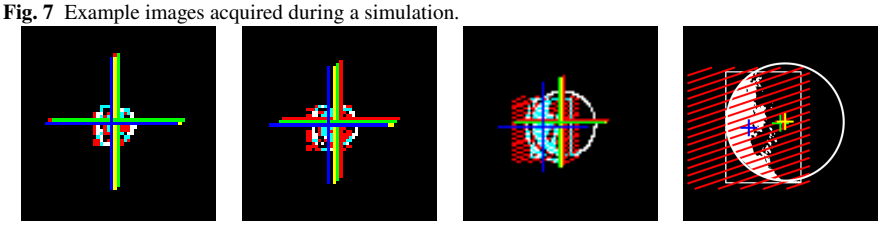

560 s, 1235 km, 10 px | 380 s, 838 km, 15 px | 200 s, 441 km, 28 px | 20 s, 44 km, 278 px

Fig. 8 Filter error and estimated 3σ for the lateral position and velocity

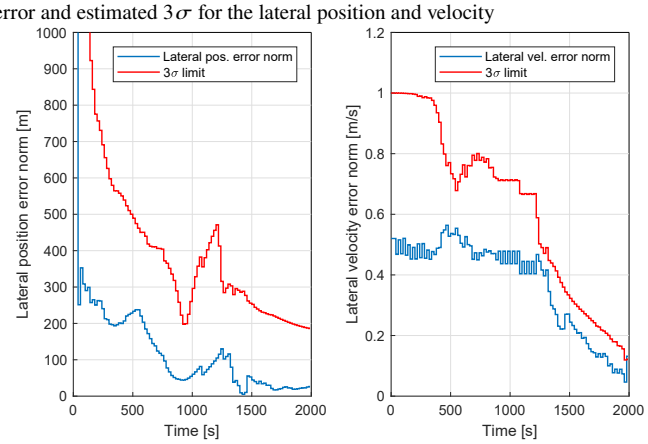

Fig. 9 Filter error and estimated 3σ for the norm of the angular velocity and the quaternion

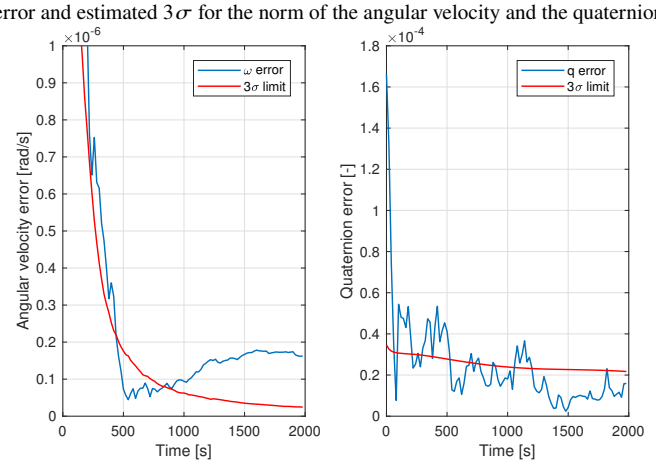

Fig. 10 Control thrust and resulting impulse

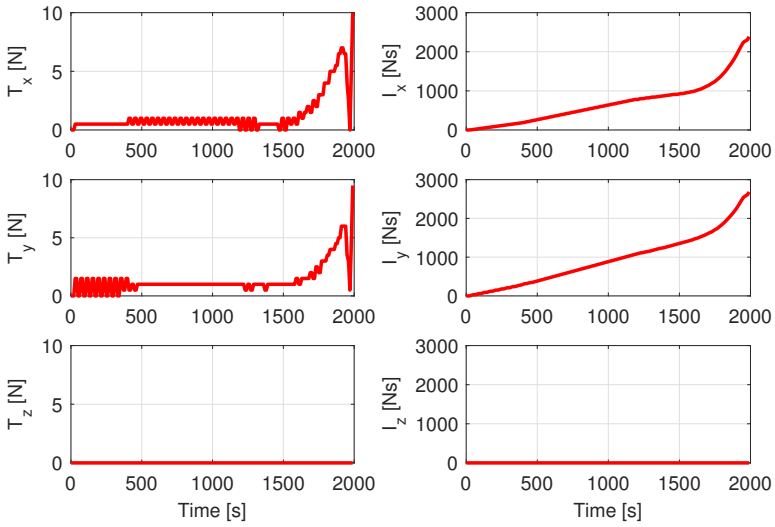

Figure 8 reports the position error perpendicular to the LOS with its estimated 3σ limit. The initial significant error decreases during the approach to the asteroid, up to a value that is sufficiently low to grant impact. The error is always below the 3σ limit, therefore the filters have given consistent results.

The rotational error and its 3σ limit are plotted in Fig. 9. Considering how a rotation quaternion is defined, its error, that remains below 1×10^{-4}, can be associated to a rotation of about 0.01 deg, that is sufficiently low to point correctly towards the asteroid. Yet, it goes beyond the 3σ limit. This result is expected to be due to the nonlinearity of the attitude equations and is left to further analysis in future work.

Figure 10 illustrates the control thrust and the resulting impulse until impact: no thrust is required along the z direction, which points towards the asteroid. This is the expected behavior of the adopted control strategy. The total impulse is 5070 Ns, with a resulting Δv of 13.7 m/s. After a transient, the torque goes to zero (see Fig. 11), which is expected since the spacecraft is moving along a trajectory almost aligned with the asteroid.

A Monte Carlo simulation is then performed to validate the model of the system and the developed GNC strategy. A set of 1000 initial conditions with Gaussian distribution is generated and used for the simulations. For each initial condition, the asteroid is rotated in a different random attitude. No angular velocity is applied to the asteroid.

At the end of the simulation, the asteroid is hit almost at his center in 99.4% of the cases, whereas it is missed in 0.2% of them. This can be seen in Fig. 12, where the green curve represents the 3σ uncertainty ellipse of the points and the asteroid is schematically drawn as a circle, with center of mass at the axes origin. Figures 15 and 16 report the distribution of the impact points against the distance from

Fig. 11 Control torque

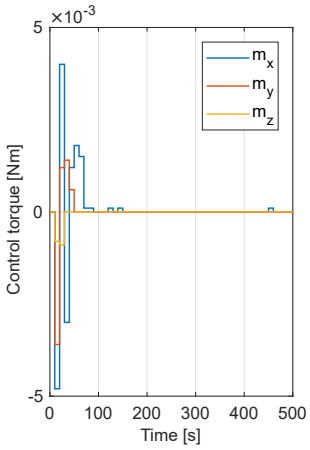

Fig. 12 Impact points with respect to the approximate size of the asteroid in Monte Carlo simulations

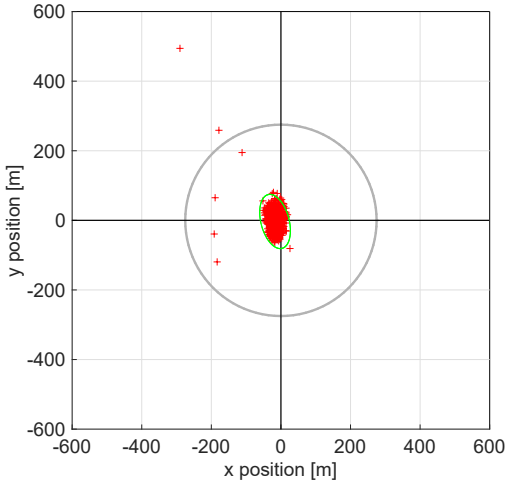

the center. Figure 13 shows the time profiles of the resulting position error in terms of norm of the perpendicular ZEM. The error decreases with time in all simulations, which confirms that the asteroid has been always detected and the control works properly. Figure 14 reports the statistical distribution of the total required Δv, showing that an average of about 10 m/s is needed.

As reported in section 3.1, a preliminary simulation using the model of asteroid Itokawa has been performed. For the sake of comparison, the asteroid model has been rescaled to have a maximum size of 550 m. Similarly to Fig. 12, Fig. 17 reports the impact points reached at the end of the approach phase on a circle of 550 m. Evidently,

Fig. 13 $ZEM_{\perp}$ behavior in Monte Carlo simulations

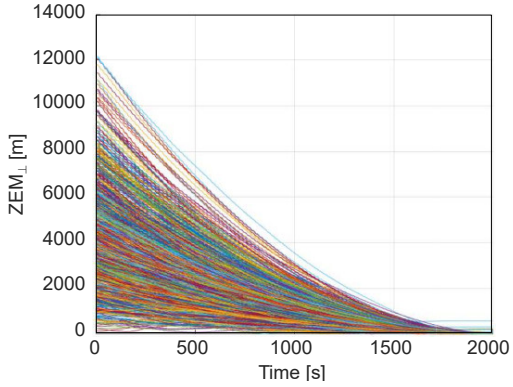

Fig. 14 Δv distribution in Monte Carlo simulations (1000 cases)

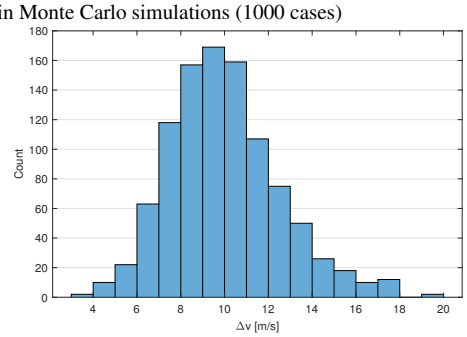

Fig. 15 Density of impact points

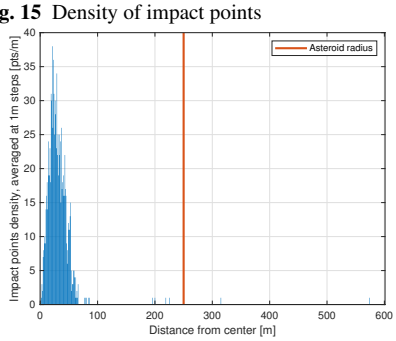

Fig. 16 Cumulative distribution of impact p.

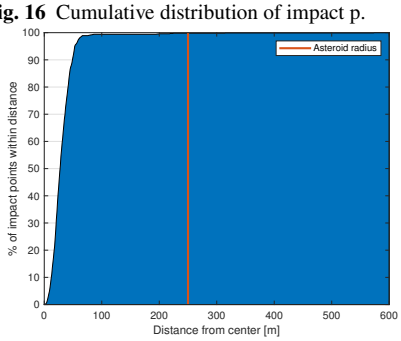

the performance of the GNC strategy performance drops drastically, due to the larger error on the identification of the asteroid center of mass.

6.2.1 Sensitivity to the size of the asteroid

To estimate the sensitivity of the proposed GNC strategy to the size of the asteroid, a Monte Carlo simulation has been performed with 100 samples and by varying the

Fig. 17 Impact points with respect to the approximate maximum size of the asteroid in Monte Carlo simulations using Itokawa

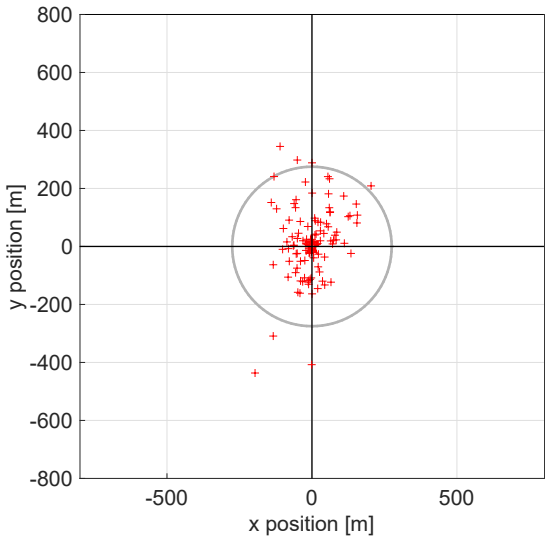

asteroid size from 25 % to 175 % with respect to the nominal value of 550 m in diameter, i.e. from 137.5 m to 962.5 m.

The results in term of impact error are reported in Fig. 18. All but the 25 % scale show similar results in absolute terms. Normalizing the distances to the asteroid size (see Fig. 19) confirms that the impact with the 25 %-scaled asteroid cannot be achieved in most cases.

Poor results are achieved also at 50 % scale and start to be sufficient at 75 %, i.e. with an asteroid of 412.5 m diameter. Then, the performance in terms of impact points relative to the asteroid size steadily improves when the asteroid is enlarged.

Fig. 18 Impact points for varying asteroid size

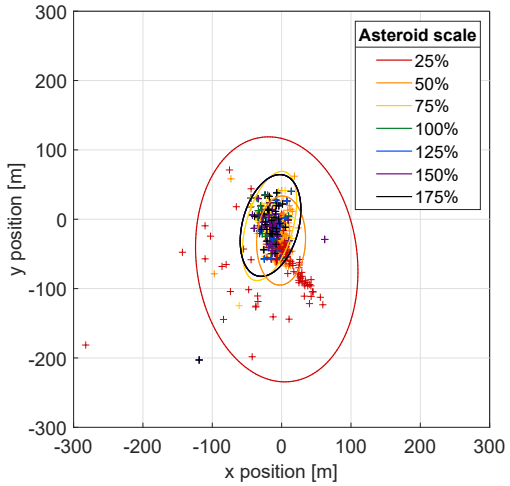

Fig. 19 Impact points for varying asteroid size with distances normalized to the asteroid radius

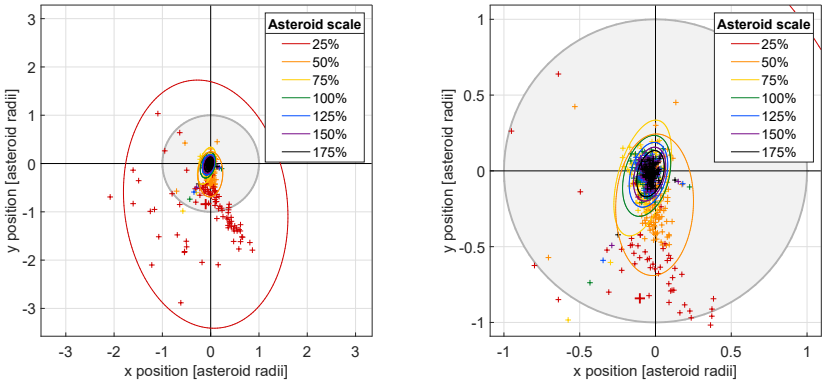

7 Conclusions and future work

The aim of this work was to design a GNC strategy for a reference impactor mission for asteroid deflection and to evaluate its performance by developing a software simulator. Within the considered initial error in position and velocity, the implemented GNC strategy shows satisfactory performance and grants impacting trajectories in almost all the simulated cases. Still, the simulated test case is very specific and it is then necessary to test the GNC strategy on different mission scenarios in future works.

Following the GNC strategy refinement, the failure cases will be carefully inspected to identify all criticalities and to propose modifications to solve or mitigate them.

The developed software is versatile: the flexibility of the Simulink® model and the possibility to tune the parameters of the system allow the user to test different mission scenarios with minor modifications.

Significant work shall be dedicated to developing a more realistic simulator. The Blender® model used to simulate the navigation camera shall be improved by implementing stars in the background and adding the effect of other phenomena that may affect the acquired image (e.g. asteroid magnitude, camera aperture, noise). Then, the performance of the image processing algorithm must be assessed with the improved rendering model.

The simulations have been performed by limiting the action of the GNC strategy to the last 2000 s before impact. Yet, some cameras are able to detect the asteroid earlier: the possibility of improving the results by executing GNC operations starting at a different time-to-impact shall be evaluated.

In addition, future work will be devoted to run the GNC strategy in a processor-in-the-loop environment to verify its on-board applicability.

Acknowledgements The authors would like to acknowledge the support provided by C. Colombo, E. Vellutini, M. Castronuovo, M. Albano, R. Bertacin, A. Gabrielli, E. Perozzi and G. Valsecchi for the definition of the test case scenario.

References

1. Berner, P., Toms, R., Trott, K., Mamaghani, F., Shen, D., Rollins, C., Powell, E.: Technical Concepts Orientation, Rotation, Velocity and Acceleration, and the SRM. Tech. rep., SEDRIS (2008). URL http://www.sedris.org/wg8home/Documents/WG80485.pdf
2. Carnelli, I., Gàlvez, A., Izzo, D.: Don Quijote: a NEO deflection precursor mission. NASA Workshop: Near–Earth Object Detection, Characterization and Threat Mitigation (2006)
3. Colombo, C., Albano, M., Bertacin, R., Castronuovo, M.M., Gabrielli, A., Perozzi, E., Valsecchi, G., Vellutini, E.: Mission analysis for two potential asteroids threat scenarios: optimal impact strategies and technology evaluation. In: 68th IAC, pp. 1–12. IAF (2017)
4. Crassidis, J.L., Junkins, J.L.: Optimal estimation of dynamic systems. CRC Press (2012)
5. Di Lizia, P., Massari, M., Cavenago, F., Wittig, A., Summerer, L.: Assessment of on-board DA state estimation for spacecraft relative navigation Final Report. Tech. rep., ESA (2017). URL https://www.esa.int/gsp/ACT/doc/ARI/ARI%20Study%20Report/ACT-RPT-MAD-ARI-16-5201-Assessment_of_onboard_DA_state_estimation_for_spacecraft_relative_navigation.pdf
6. Drube, L.: SMPAG Roadmap of Relevant Research for Planetary Defense. Tech. rep., SMPAG (2018). URL https://www.cosmos.esa.int/documents/336356/336472/SMPAG-RP-001_2_0_Roadmap_2017-10-11.pdf
7. Gàlvez, A., Carnelli, I., Michel, P., Cheng, A.F., Reed, C., Ulamec, S., Biele, J., Abell, P.A., Landis, R.: AIDA: The Asteroid Impact & Deflection Assessment Mission. European Planetary Science Congress (2013). URL http://meetingorganizer.copernicus.org/EPSC2013/EPSC2013-1043.pdf
8. Guo, Y., Hawkins, M., Wie, B.: Applications of Generalized ZEM/ZEV Feedback Guidance Algorithm. Journal of Guidance, Control, and Dynamics **36**(3), 810–820 (2013). DOI 10.2514/1.58099
9. Hawkins, M., Guo, Y., Wie, B.: ZEM/ZEV Feedback Guidance Application to Fuel-Efficient Orbital Maneuvers Around an Irregular-Shaped Asteroid. In: AIAA GNC Conference (2012). DOI 10.2514/6.2012-5045
10. Kubitschek, D.G., Mastrodemos, N., Werner, R.A., Kennedy, B.M., Synnott, S.P., Null, G.W., Bhaskaran, S., Riedel, J.E., Vaughan, A.T.: Deep Impact autonomous navigation: The trials of targeting the unknown. In: AAS, vol. 125, pp. 381–406. JPL, NASA (2006). DOI 2014/38755

11. Kubota, T., Hashimoto, T., Kawaguchi, J., Uo, M., Shirakawa, K.: Guidance and Navigation of Hayabusa Spacecraft for Asteroid Exploration and Sample Return Mission. In: 2006 SICE-ICASE International Joint Conference, pp. 2793–2796. IEEE (2006). DOI 10.1109/SICE.2006.314761
12. Schaub, H., Junkins, J.L.: Analytical mechanics of space systems. AIAA (2003). DOI 10.2514/4.861550
13. Woodbury, D., Junkins, J.L.: On the Consider Kalman Filter. In: AIAA GNC Conf. (2010). DOI 10.2514/6.2010-7752